Spring 5-19-2014

Monte Carlo Simulations of Atmospheric Loss by Stellar Winds from Exoplanets

Daniel Violette
University of Connecticut - Storrs, daniel.violette@uconn.edu

Monte Carlo Simulations of Atmospheric Loss by Stellar Winds from Exoplanets

Daniel Violette
University of Connecticut, Department of Physics

Abstract

Hot Jupiters are a class of extra-solar planets. Massive gas giants on the same size scale as Jupiter, they orbit their host stars closely. This proximity results in large stellar winds capable of stripping away a planet's atmosphere. Developing a more complete understanding of atmospheric mass loss and evolution in planetary bodies is critical, and Hot Jupiter systems are accessible analogues.

This project will seek to create a computational model capable of estimating mass loss rates due to stellar winds. A Monte Carlo method is utilized to take an ensemble of single, high-energy energetic neutral particles, produced by kilo-electronvolt stellar wind ions, and and trace their path through theoretical atmospheres. As these particles travel, they collide many times, imparting energy to the atmospheric molecules and potentially exciting them to high enough energies to escape the planetary gravity. Different mechanisms for particle interaction and escape will also be analyzed in order to determine their impact on the mass loss rates. Overall, this modelling method can be used to predict the effects of variables on the flux of escaping particles for different parametric families of observed hot Jupiters.

Acknowledgements

Daniel would like to thank Dr. Vasili Kharchenko and Nick Lewkow of the UConn Department of Physics for their invaluable guidance and support throughout the project. Daniel would also like to thank the UConn Physics Department for the resources it provided. Finally, Daniel would like to thank the UConn Honors Department and University Scholar Program.

Table of Contents

List of Figures

List of Tables

1 Introduction and Theory

1.1 Discovering Exoplanets

The concept of cosmic pluralism, or the existence of other worlds similar to our own, has existed throughout written history. It is a theory that was explored and supported by brilliant thinkers, philosophers and scientists, including Democritus, the ancient Greek who is thought by some to be the father of modern science[1], and Giordano Bruno, an Italian priest who's early adaption of the Copernican model and works on the idea of an infinite universe led to his excommunication and execution[2]. Other influential scientific thinkers explored the theory, including Sir Isaac Newton, William Herschel, Benjamin Franklin, Frank Drake, and Carl Sagan, among others. However, it wasn't until very recently—the mid-1990s to be more exact[3,4]—that scientific observational data proved the existence of planetary bodies outside of our solar system.

An extrasolar planet, or exoplanet, is defined as any planetary body that exists outside our solar system and orbits another stellar body. The initial discoveries of these exoplanets were heavily debated and alternate theories were proposed to explain the data[5]. However, with the development of improved detection equipment and techniques the existence of exoplanets has been widely accepted in the scientific community. In fact, technological innovations such as the Kepler Space Telescope has accelerated exoplanet candidate discovery in recent years. According to the Extrasolar Planet Encyclopedia, 1781 planet candidates have been identified to date[6]. Surveys performed on the exoplanetary data collected to date has led to an astounding estimate; each star in the Milky Way Galaxy is estimated to host 1.6 exoplanets[7]. In just over two decades of active observational data collection and research, Cassan et al. was able to conclude in *Nature* "that stars are orbited by planets as a rule, rather than the exception[7]". The discovery and identification of so many different exoplanets has led to the development of a flourishing academic field that focuses on the study of planets and exoplanets, including their composition, formation, evolution, and lifetimes.

Several different methods of detection have been utilized to identify possible exoplanet candidates. The first and most heavily utilized method is the "Doppler Wobble" or radial velocity measurement method[8]. As a large exoplanet orbits its parent star, its gravitational pull causes the star to circle around a central point itself. If the harmonic motion is in the correct plane, the star will appear to oscillate between moving towards earth and moving away from earth. This "wobble" blue-shifts star light as the star approaches us and red-shifts light as the star moves away. Utilizing spectroscopy, the orbital period of the star around the center of mass of the planet-star system can be inferred, along with information about the orbiting exoplanet. Transiting exoplanets is another heavily utilized detection method that has become more useful with the introduction of better instruments, such as the Kepler Space Telescope[4,9]. By pointing a telescope statically at a star, it is possible to note a relative change in flux of light coming from the star when a planet passes directly in front of it. The first transits were quickly spotted by the beginning of the year 2000[10]. By analyzing this change in flux, it has become possible to predict

the planet's size, orbital period, and semi-major axis, along with the important ability of being able to detect the presence of exoplanetary atmospheres. Other useful detection methods include gravitation lensing, a situational tool that often does not allow for repeated measurements, and direct imaging, which has been difficult in the past but may become a more significant technique with the introduction of the next generation of space and ground based telescope. In the next decade the introduction of a new generation of telescope including NASA's James Web Space Telescope and the European Extremely Large Telescope in Chile will again expand our capabilities by allowing us to detect smaller and colder exoplanets[4].

1.2 Exoplanetary Atmospheres

The first direct detections of exoplanetary atmospheres in 2002 were discoveries that carried as much significance as the first observations of exoplanets[11]. By noting the differences in the stellar spectra of a star before and during an exoplanetary transit event, it is possible to determine the composition of exoplanet atmospheres. Many models have been developed in order to attempt to explain the possible dynamics present in these extrasolar bodies. These models often derive most of their theoretical basis from atmospheric models of the earth and other planets in our solar system. By utilizing fluid dynamics, temperature-pressure profiles, convective, radiative and hydrostatic equilibrium, gas laws, and conservation laws, planetary scientists and astrophysicists attempt to understand atmospheric conditions of exoplanetary bodies light-years away[4].

Exoplanetary atmospheres are just as varied as the exoplanets they belong to and are affected by a myriad of conditions. The atmospheric composition of exoplanets is largely dependent on the planet's surface temperature, size, mass, semi-major axis (which affects temperature, and at small values can cause tidal forces and tidal locking), and the elemental and molecular species present[12]. Exoplanet atmospheres can be categorized in five groups in order to attempt to simplify understanding[4]. The groups are: Hydrogen and Helium dominant, which are formed from the protoplanetary nebula, outgassed atmospheres dominated by hydrogen, outgassed atmospheres dominated by carbon dioxide, hot super earth atmospheres which lack volatiles due to high temperatures (with surface temperatures usually over 1500K), and atmosphere-less rocky planets due to atmospheric escape mechanisms.

1.3 Atmospheric Escape

When discussing the evolution study of exoplanetary atmospheres, one very active field of research is the study of evaporation (or mass loss) due to interaction with stellar winds[13]. Stellar wind is the plasma flux composed of electrons and high energy ions emitted by a star which can interact with neutral atomic and molecular gases in an exoplanetary atmosphere. This interaction can cause these gases to escape from the planet's gravitational field. This can effectively "sweep" away the atmosphere of a planet. The atmosphere-stellar wind interaction can be direct if the planet does not have a strong magnetic field. Additionally, this interaction may happen via planetary magnetospheric ions, if the planet possesses a magnetic field. For

example, a prevailing theory claims that Mars once had an atmosphere protected by a magnetic field much like Earth's. Mars' magnetic field became unstable, baring the atmosphere to interactions with the solar wind. This led to much of the atmosphere being stripped away[14].

Energetic Neutral Atoms (ENAs), precipitating into planetary atmospheres can be formed through charge exchange collisions when stellar wind plasma interacts with colder gases, such as magnetospheric ions[15,16]. These ENAs do not interact with the magnetic field and have energies orders of magnitude higher than the local thermal environment. ENAs are capable of penetrating deep into atmospheres, colliding with thermal atmospheric atoms and molecules and creating high-energy Secondary Hot Particles (SHPs). The precipitation of ENAs in an exoplanetary atmosphere can potentially excite SHPs to large enough energies to escape a planet's or exoplanet's gravitational potential. Over time and under certain conditions, this atmospheric mass loss may accumulate and lead to large escaping gas fluxes not previously explained by other escape mechanisms like thermal Jean's escape[12].

Hot Jupiters, extrasolar gas giants which are usually located close to their hosting stars, serve as additional examples for this type of extreme atmospheric loss[4]. Many Hot Jupiters rotate so closely around their stars that they can complete a full rotation in mere days and have semi-major axes on the order of 0.01 AU. The extrasolar wind intensity incident on these giants is immense due to their extreme stellar proximity. Additionally, the Roche limit created by tidal forces from nearby celestial bodies can reduce the particle's escape energy requirements[17]. It is still not clear how long these atmospheres can withstand such punishment. Already several Hot Jupiters have been identified that possess extended escaping atmospheres that have measurable mass loss rates, namely HD 209458 and HD 189733b[18,19].

Developing a more complete understanding of atmospheric mass loss is crucial. Atmospheres are necessary for most forms of life, and understanding how they change and evolve will not only provide insights into atmospheric lifetimes on distant worlds but will also paint a clearer picture of how atmospheres in our solar system have evolved. In order to further these ends, a computational Monte Carlo model was created with the intent of analyzing the effects of intense ENA fluxes on a simplified planetary atmosphere in order to develop an understanding of the effects that stellar winds can have on exoplanetary atmospheres.

2 Theoretical Foundation

2.1 Thermalization Energy Derivation

In an atmospheric model of ideal gases, particles can be considered to exist at thermal equilibrium[20]. Utilizing statistical mechanics and thermodynamics, the energy of individual particles at thermal equilibrium can be easily calculated. Although the majority of the processes in the planetary evolution can be treated classically, the atmospheric energy relaxation and escape processes have to include a quantum-mechanical consideration. The necessary quantum approach arises because the energy transfer processes in collisions of atmospheric atoms and molecules with ENAs and stellar wind ions are quantum mechanical by nature. Quantum results are therefore used to derive the non-thermal escape rates.

To find the average thermal energy of an ideal gas, the case can be considered of one atom of mass M in a 3-D box of volume V = L^3. Outside the box the wave function of the particle is zero[21]. Inside the box, the wave function can be described by the three-dimensional harmonic oscillator equation.

$$-\frac{\hbar^2}{2m}\nabla\psi = -\frac{\hbar}{2m}\left(\frac{\mathrm{d}^2}{dx^2}+\frac{d^2}{dy^2}+\frac{d^2}{dx^2}\right)\psi = E\psi \tag{1}$$

Utilizing the boundary conditions where the wave function of the particle is zero everywhere except within the box (between –L/2 and L/2 in all dimensions), the allowed energy of the system can be calculated. Unlike classical physics, only certain quantized energy levels are allowed.

$$\epsilon_n = \frac{\hbar^2}{2M}\left(\frac{\pi}{L}\right)^2\left(n_x^2+n_y^2+n_z^2\right) \tag{2}$$

Next, the partition function Z(τ), a summation over the Boltzmann factor, is used to calculate the probability that the atom in the box is at a particular energy level[20].

$$Z(\tau) = \sum_n \exp\left(-\frac{\epsilon_n}{\tau}\right) \tag{3}$$

$$P(\epsilon_n) = \frac{\exp\left(-\frac{\epsilon_n}{\tau}\right)}{Z} \tag{4}$$

The average thermal energy of a single atom or particle is defined as

$$E_{therm} = <\epsilon> = \sum_n \epsilon_n P(\epsilon_n) = \sum_n \frac{\epsilon_n \exp\left(-\frac{\epsilon_n}{\tau}\right)}{Z}$$

The average thermal energy per particle of a 3-dimensional homogeneous ideal gas is

$$E_{therm} = \frac{3}{2}KT = \frac{m}{2}v_{rms}^2 \tag{6}$$

This result, which is a valid in both quantum and classical gas motion approximations, is significant for this project. By understanding the thermal energy of individual particles in an atmosphere it is possible to calculate distinct limits for SHP creation and ENA thermalization. This result also shows how the model will be dependent on the surface temperature selected.

2.2 Escape Energy Derivation

In the computational model, particles will regularly be energized to high enough energies to potentially escape the atmosphere in the form of secondary hot particles (SHPs). While it is a rough approximation, the velocity these particles will require to escape can be calculated by starting from newton's law of universal gravitation [22]. When the gravity of a planet of mass *M* acts on a particle of mass *m*, the force can be calculated by

$$\vec{F}_G = -\frac{GMm}{|\vec{r}|^2}\hat{r} \tag{7}$$

Since F_G is a conservative force, the relationship between the force and the associated potential energy *U* is

$$U(r) = -\int_r^\infty F_G(r') \cdot dr' = GMm\int_r^\infty \frac{1}{r'^2}dr' = -\frac{GMm}{r}$$

Therefore a particle that has a speed capable of allowing for escape must additionally have a kinetic energy with a magnitude greater than that of the associated gravitational potential.

$$E_{esc} \geq |U(r)| = \frac{GMm}{r} = \frac{m}{2}v_{esc}^2 \tag{8}$$

Finally, calculating escape velocity,

$$v_{esc} = \sqrt{\frac{2GM}{r}} \tag{9}$$

The significance of this result is that it reveals what parameters are important when calculating the probability that an SHP will escape a modelled atmosphere. Therefore, the escape flux will be heavily dependent on planetary mass and SHP creation altitude.

2.3 Hard Sphere Collision Cross Sections

Classically, collisions of particles can be considered to be between solid hard spheres (HS) like pool balls in a game of billiards. Collision probability relies heavily on target *cross sections*, or the area of any one target perpendicular to the incident direction of the moving projectile[22]. This simple model of collision doesn't explain the process of collisions between particles such as atoms and molecules as well as a quantum mechanical theory does, but it is a less complex model that can be applied much more easily. Therefore, the mechanics of HS

collisions will be explored in order to demonstrate primary collisional theory that was used in the project.

Consider a spherical projectile and target with radii R_p and R_t respectively. In order for the projectile and target to collide, the distance between the center of the two spheres, the *impact parameter* b, must be less than the sum of the radius of the two spheres. If the combined radius of the two spheres ($R = R_p + R_t$) is less than the impact parameter, than no impact will occur (Fig. 1). Another way to think about this is that the projectile will collide with the target if it enters into a circular cross section perpendicular to the direction of projectile motion of radius R. Following this thinking, calculating the target cross section σ_{HS} becomes straight forward:

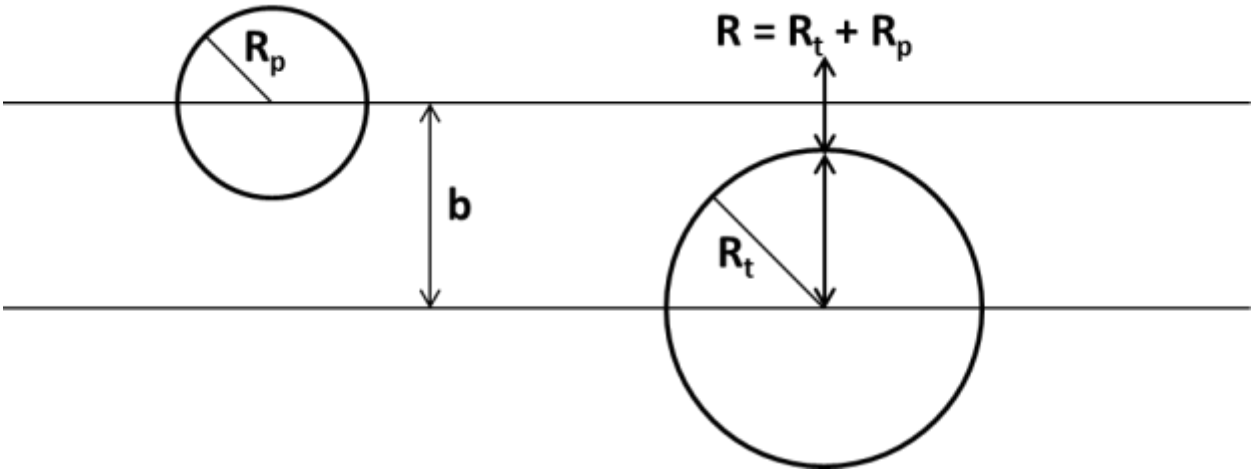

Figure 1 – Hard sphere collision with relevant values of impact parameter b and target cross section R.

$$R = R_p + R_t \tag{10}$$

$$\sigma_{HS} = \pi R^2 = \pi\left(R_p + R_t\right)^2 \tag{11}$$

Collision when: $b \leq R = R_p + R_t$

Therefore, the HS collisional cross section increases as a function of the radius squared. Larger atmospheric and projectile particles yield larger collisional cross sections. Additionally, HS cross sections are independent of projectile and target energy, further simplifying calculations. Finally, hard sphere scattering is isotropic in the center of mass frame. This means that all scattering angles have an equivalent probability in the center of mass frame and can be randomly generated in the Monte Carlo model.

2.4 Mean Free Path Calculations

Generalizing the HS collision cross section result to a gas comprised of many small spherical balls, the *mean free path* λ, or the average distance traveled between consecutive impacts, can be calculated[22]. If the projectile particle is very energetic, the motion of thermal atmospheric particles can be neglected in favor of simplifying the model to stationary atomic targets. The projectile molecule or atom travels through a cloud of stationary particles and will

travel a distance of y before colliding with one of these particles. If we take a thin slice of the cloud that the projectile is traveling through with thickness dy, then the target density (number of targets per area) n_{tar} of this slice can be calculated:

$$n_{tar} = \frac{N}{V} dy = n dy \tag{12}$$

The number density of the gas n is N/V, where N is the number of gas particles and V is the volume the gas particles fill. The total number of targets is represented by $n_{tar}A$, where A is the total cross sectional area that the projectile may pass through, and the total area of all the targets is $n_{tar}A\sigma$. The probability of a collision $P_{collision}$ within an infinitesimal slice dy can now be found which leads to a calculation of mean free length.

$$dP_{collision}(dy) = \frac{A_{occupied}}{A} = \frac{n_{tar}A\sigma}{A} = n_{tar}\sigma = n\sigma dy \tag{13}$$

The probability that a particle between the current position y and the next thin slice dy will collide $dP_{collision}(\text{y to y} + \text{dy})$can be calculated from the product of the probabilities of a collision in dy, $dP_{collision}(dy)$, and the probability that a collision will not occur through length y, $P(y)$.

$$dP_{collision}(\text{ y to y} + \text{dy}) = P(y) * P_{collision}(dy) = P(y) * n\sigma dy \tag{14}$$

$P_{collision}(y)$ is related to $P(y)$ by

$$P_{collision}(y) = 1 - P(y)$$

Therefore, the probability of a collision between length y and $y + dy$ can be additionally written as the chances that a particle will scatter in length $y + dy$ and subtract the probability that a particle will collide in length y.

$$dP_{collision}(\text{y to y} + \text{dy}) = P_{collision}(y + dy) - P_{collision}(y)$$

Re-writing in terms of the probability that a particle will not collide

$$dP_{collision}(\text{y to y} + \text{dy}) = P(y) - P(y + dy) = -\frac{d}{dy}P(y)dy \tag{15}$$

Setting equations 14 and 15 equal to each other, $P(y)$ can be found.

$$\frac{d}{dy}P(y) = -n\sigma P(y)$$

$$P(y) = e^{-\left(\frac{N\sigma}{V}\right)y}$$

The mean free path of the system is defined as the average distance the particle will travel between consecutive collisions. Therefore, the mean free path is a product of a distance y and the distance the particle collides between y and dy.

$$\lambda = \langle y \rangle = \int_0^\infty y \, dP_{collision}(\text{y to y + dy})$$

$$\lambda = \int_0^\infty y \, [n\sigma P(y)] dy = \int_0^\infty y \left[n\sigma e^{-\left(\frac{N\sigma}{V}\right)y} \right] dy$$

$$\lambda = \frac{1}{n\sigma} \tag{16}$$

Utilizing this result for the mean free path, it can be seen that the distance between collisions increase as the cross sections of the atmospheric particle and the density of the target gas increases, both of which make intrinsic sense.

2.5 Elastic Collision Energy Transfer

In the developed model, particles collide in a simplified *elastic* model. This means that all energy and momentum is conserved in the collision process and no energy is lost due to internal states[23]. Therefore, the energy transfer process that occurs when particles collide can be solved utilizing momentum and energy conservation principles.

Starting in the center of mass frame of colliding particles and treating the two particles as traveling towards each other with equal and opposite momenta, the collision between the two particles rotates the momentum vector (Fig. 2). By assigning a unit vector *k* as the velocity vector of the projectile following the collision, then the velocities of the projectile and target following the collision, v_{pf} and v_{tf}, can be written as functions of the target and projectile mass which are m_t and m_p respectively.

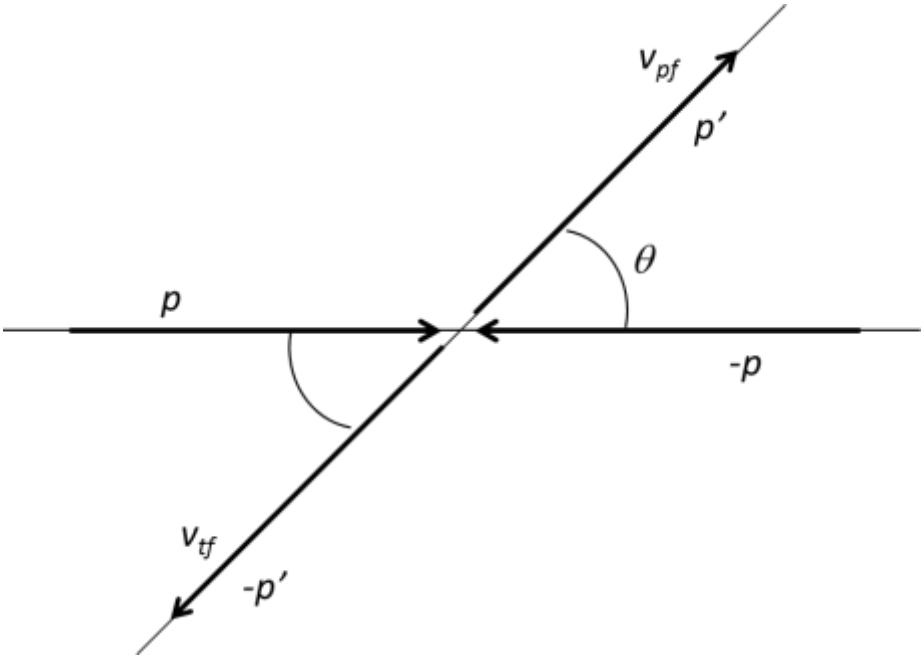

Figure 2 – Center of mass scattering of a projectile (right) and target particle (left) traveling with momenta p with center of mass scattering angle θ. Particles scatter with momenta p'.

$$v_{pf} = \frac{m_t vk}{m_t + m_p} \tag{17}$$

$$v_{tf} = -\frac{m_p vk}{m_t + m_p} \tag{18}$$

The velocity of the projectile can be converted back to the lab frame by adding the velocity of the center of mass to each equation.

$$v_{pf} = \frac{m_t vk}{m_t + m_p} + \frac{m_p v'_{pi} + m_t v'_{ti}}{m_p + m_t}$$

Assuming one of the particles is at rest the equation can be further simplified. Considering the case where two HS particles collide, the velocity results can be treated geometrically. Utilizing Newton's diagram for the particle momenta (Fig. 3), the relationship between scattering angles can be simplified from the angle the direction of impact and directions of motion of the projectile after the collision χ_p to the angle which the projectile is deflected in the center of mass frame θ geometrically.

$$\tan(\chi_p) = \frac{m_t \sin(\theta)}{m_p + m_t \cos(\theta)}$$

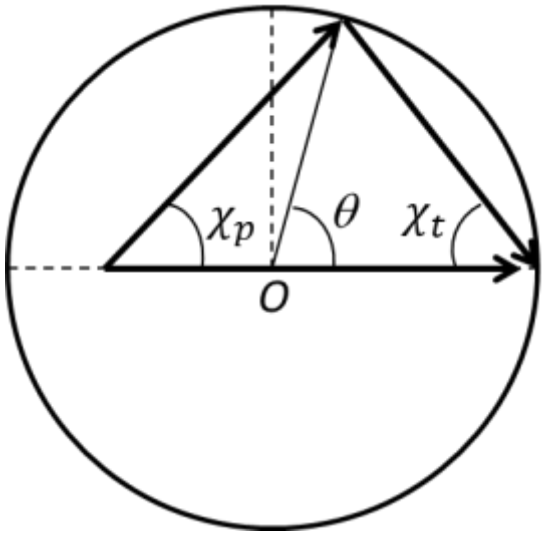

Figure 3 – Newton's diagram for particle momenta of collision of the center of mass scattering from θ as well as the direction of motion angles after collision of the projectile and target χ_p and χ_t.

Applying this geometric relationship, the magnitude of the velocity of the projectile can be expressed in terms of θ[23].

$$v_{pf} = v\left(\frac{\sqrt{m_p^2 + m_t^2 + 2m_p m_t \cos(\theta)}}{m_t + m_p}\right) \tag{19}$$

Writing this relationship in terms of energy, and defining $\rho = \frac{m_p}{m_t}$, the final energies of the scattered target and projectile particles are solved.

$$E_{pf} = \frac{1}{2}mv_{pf}^2 = E_0\left(\frac{1 + 2\rho\cos\theta + \rho^2}{(1+\rho)^2}\right); \rho = \frac{m_p}{m_t} \tag{20}$$

$$E_{tf} = E_0 - E_{pf} \tag{21}$$

2.6 Stellar Flux Parameters

To finish the section, basic flux calculations are performed to show why stellar wind induced ENAs are potential causes of high rates of mass loss. Consider that a ninth planet was discovered in our solar system. This planet is the same size as earth but orbits extremely close to the sun at 0.005AU. This distance is comparable to the proximity of several identified exoplanets to their host stars[6]. At this distance from the sun, this new planet is much closer than even mercury which orbits at 0.307 AU, and makes full rotations of the sun in less than a day.

In order to compare the solar wind flux incident on earth and this imaginary new planet, consider that the total flux *J* emanating from a central point remains constant (*K*) as a function of the spherical surfaces *S* the flux can be said to be passing through. .

$$JS = K$$

This means that the total solar wind flux passing through a spherical shell at R = 1AU at the Earth is equal to the total flux passing through a spherical shell R = 0.005AU.

$$J_{Earth}S_{earth} = J_{New}S_{New}$$

From this relationship, the flux incident on the new planet can be calculated.

$$J_{New} = J_{Earth}\frac{S_{Earth}}{S_{New}} = J_{Earth}\frac{4\pi R_{Earth}^2}{4\pi R_{New}^2}$$

$$J_{New} = J_{Earth}\frac{R_{Earth}^2}{R_{New}^2} = J_{Earth}\frac{1^2}{0.005^2}$$

$$J_{New} = 4x10^4 * J_{Earth} \tag{22}$$

The solar wind flux the new planet experiences is over four orders of magnitude greater than what we experience on Earth. This lends credibility to the idea that intense stellar wind can cause significant mass loss in exoplanets with small semi-major axes.

3 Computational Model

3.1 Basic Simulation Objectives

This computational model is designed to simulate an extreme flux of ENAs interacting with an atmospheric cloud of gases. ENAs traveling at high speeds are injected into a modelled atmosphere one by one. The ENAs are propagated through an iterative transport process. For each step of the transport, position and velocity vectors are recorded. The mean free path is re-calculated from the local density of the atmosphere, which is a function of particle height above the planetary surface, and collision cross section. These results are then used to determine a collision probability and compare it to a randomly generated value. The ENA projectile either continues to travel in a straight line or is scattered in a random direction, elastically transferring energy to a once-stationary target. If the transferred energy is greater than the escape energy of the atmosphere, a SHP is created and its position and velocity vectors are recorded to determine the escape probability. This process continues tracking the ENA until it meets specific exit criteria. Ultimately, the purpose of the model is to determine how many ENAs are reflected or thermalized (reduced to atmospheric thermal energy), as well as estimate SHP atmospheric escape fluxes (Fig. 4).

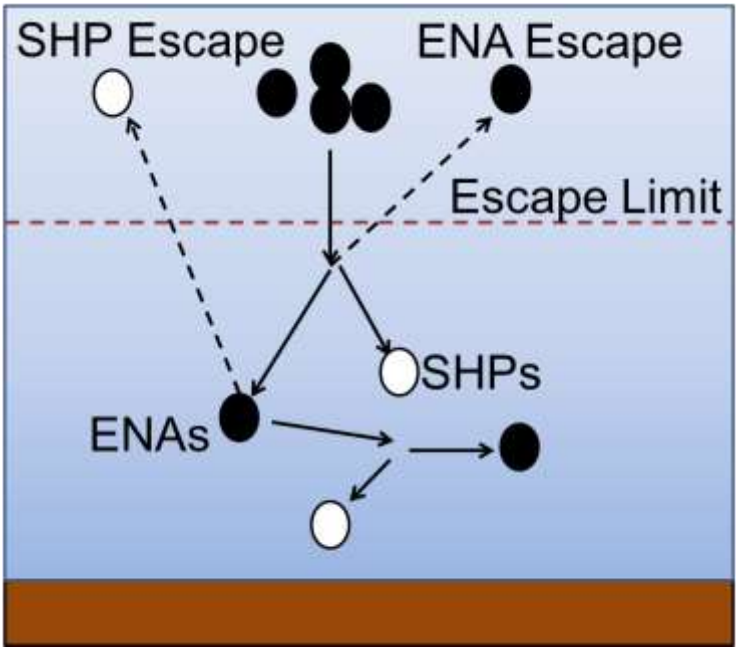

Figure 4 – Basic representation of the Monte Carlo model including ENA and SHP escape and thermalization.

3.2 Monte Carlo and Model Structure

Monte Carlo (MC) is an analysis technique that uses iterative and repeating numerical calculations to approximate a population mean from a sample mean[24]. In essence, MC is a type of computer-run statistical sampling. A simulation is run repetitively until enough data is

collected to yield statistically significant results. This computational process is used very successfully in this numerical experiment. By performing random walk statistics on a particle projectile as it travels through an atmosphere, recording the results, then repeating the MC simulations for a large number of particles, statistical averages and conclusions can be extracted from the data, yielding significant results. The MC method is such a powerful tool because it allows for the application of simple physical principles, like hard sphere particle collisions, to much more complex situations.

In this experiment, MC methods were utilized to solve the problem of atmospheric mass loss due to precipitating ENAs formed by stellar winds. These ENAs interact with thermal atoms within a target atmosphere elastically, creating highly energized SHPs. These SHPs have enough energy to potentially escape the gravitational potential of the host planet or exoplanet, escaping off into space. If such an escape event happens often enough, a significant mass loss rate can be calculated. The computational model was designed around a logic structure seen in Figure 5 which simply and efficiently breaks down and explains the structure of the simulated atmospheric model.

The model begins by setting initial parameters, including exoplanetary statistics like mass, atmospheric composition, and atmospheric density, ENA parameters, such as initial energy, chemical species, solar zenith angle, number of particles, and initial height. Next, each ENA is individually and incrementally transported through the atmosphere. After each step, the mean free path is recalculated based on the atmospheric model as a function of height. A random number r between 0 and 1 is then generated and checked against a probability calculated from the mean free path λ and the traveled step L.

$$P_{NoCollision} = \exp\left(-\frac{L}{\lambda}\right) \tag{23}$$

If the random number generated is smaller than the mean free path, then the fast projectile particle continues to travel in a straight line. As the particle penetrates more deeply into the atmosphere, the mean free path decreases and the probability for a collision increases. Once a collision occurs, it's updated collision location along the interval L is calculated.

$$Lx = -\lambda \log(r) \tag{24}$$

Once a particle collision occurs, random scattering angles are **g**enerated based off of the hard sphere collision model. In the center of mass scattering frame, all hard sphere scattering angles are equally as likely[20]. These angles are then utilized to find the new projectile energy E_{new} and determine if a secondary hot particle was created. An SHP is created if the energy transferred E_t is greater than the escape energy of the atmospheric system. E_{new} and E_t are calculated utilizing the developed theory in section 2.5

$$E_{New} = \frac{1}{2} m v_{ENA}^2 = E_0 \left(\frac{1+2\rho\cos\theta+\rho^2}{(1+\rho)^2}\right) ; \rho = \frac{m_{ENA}}{m_{ATMO}} \tag{25}$$

$$E_t = E_0 - E_{New} \tag{26}$$

SHP information is recorded and the ENA transportation speed and position is updated based off of these calculations. The simulation continues until any of a specific set of exit criteria is met. Once the simulation registers that the ENA has reached an exit criteria, the transport of the ENA is terminated and all values are then reset to the initial parameters. Calculations are then repeated for another ENA until reaching the number of total particles tested.

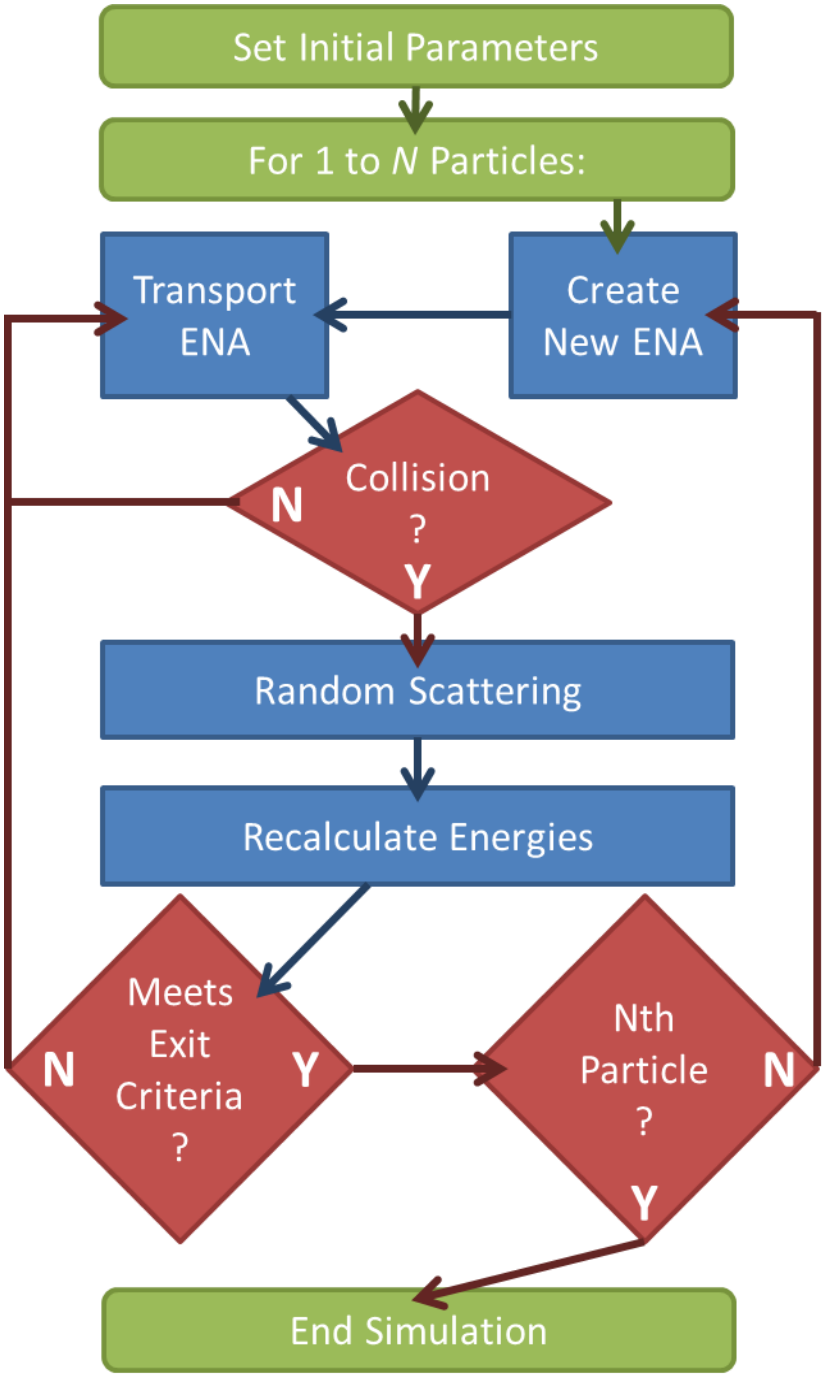

Figure 5 – Flow diagram of MC simulation testing procedure for evaluating N incident ENAs.

3.3 Initial Parameters

Initial parameters must be specified for both the exoplanet and the incident ENAs. The model of the exoplanet was based off of properties of planets found within our solar system. For modeling the Earth-like exoplanetary atmospheres, analogs including atmospheric models of Earth, Mars, or Venus could be used. For example, the altitude dependent atmospheric density model were developed from known atmospheric compositions of Mars at solar minimum (Fig 6)[25,26]. The carbon dioxide (CO2) altitude dependent density was primarily used for the model due to its high concentration density at low altitudes. Hydrogen was chosen as the primary atmospheric species due to simplifications it created in the modelling system.

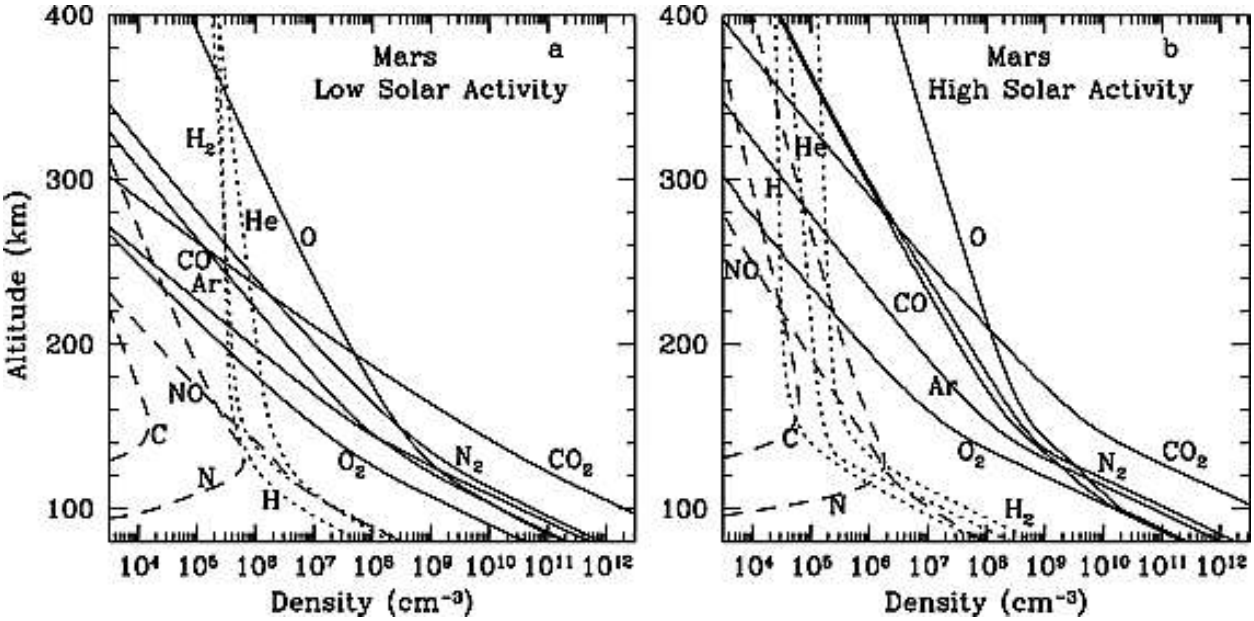

Figure 6 – Mars' atmospheric density of different species at low solar activity (left) and high solar activity (right)[26].

The ENA parameters were based off of prior ENA production calculations and solar wind measurements. The main component of the solar wind is hydrogen ions with a density of $n = 5$ cm^{-3} traveling at speeds approaching 450km/s[27]. These ions are transformed into ENAs in charge-exchange collisions with neutral atmospheric atoms. ENAS into a planet's atmosphere, with an energy distribution between 0.1eV-1keV[15] with corresponding velocities. The ENA velocity spectrum was created with a cumulative probability function, which shows that for a given probability, the ENA's initial velocity will be found to be less than or equal to some value. (Fig. 7). These ENAs are generated high in the atmosphere at atmospheric concentrations (~$1x10^5$ cm^{-3}) with negligible collision probabilities. The incident ENA angle normal to the altitude axis is additionally set to 0 to represent direct collisions of ENA particles with the planetary model's equator. Finally, the number of ENAs chosen is significant. When developing the model, the number of Monte Carlo particles (MCPs) ranged around one thousand individual particles and below. However, to reduce measurement error data-gather simulations utilized MCP counts above one million.

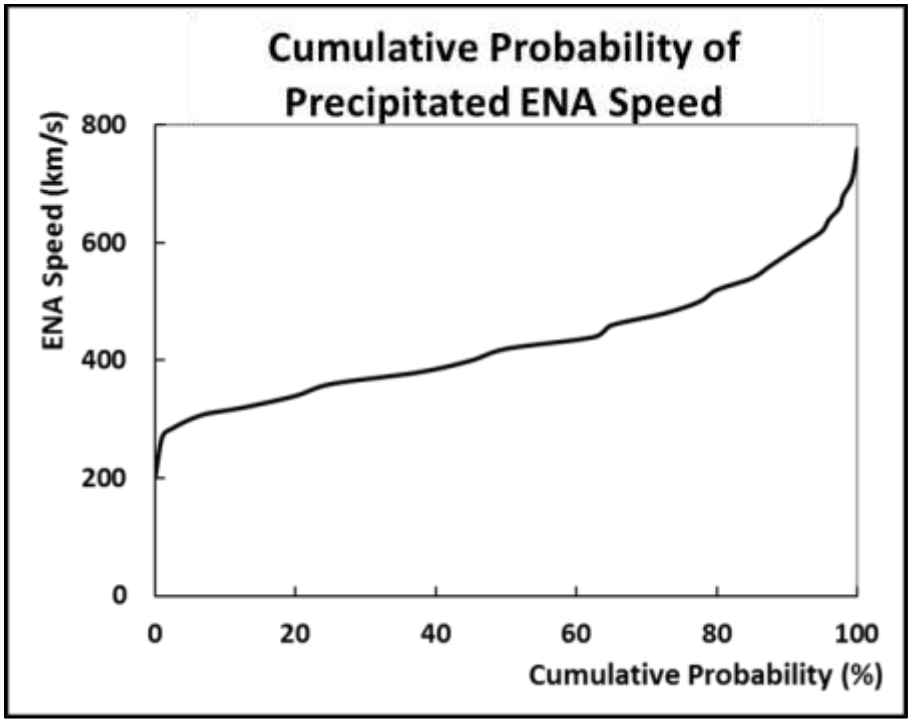

Figure 7- Cumulative probability function for ENA speed utilized in MC model.

Finally, preliminary testing was also performed utilizing slightly different scattering models. In order to more closely approximate quantum collisions, a preferentially directed scattering model was introduced utilizing a probability density function (PDF). By introducing a normalized angular Gaussian function, a random number was generated and used to find a weighted scattering angle from a cumulative probability function (CPF) (Fig. 8). This preferentially created scattering angle replaced the previously uniform HS probability density function that treated all scattering chances as equal and was compared against HS results.

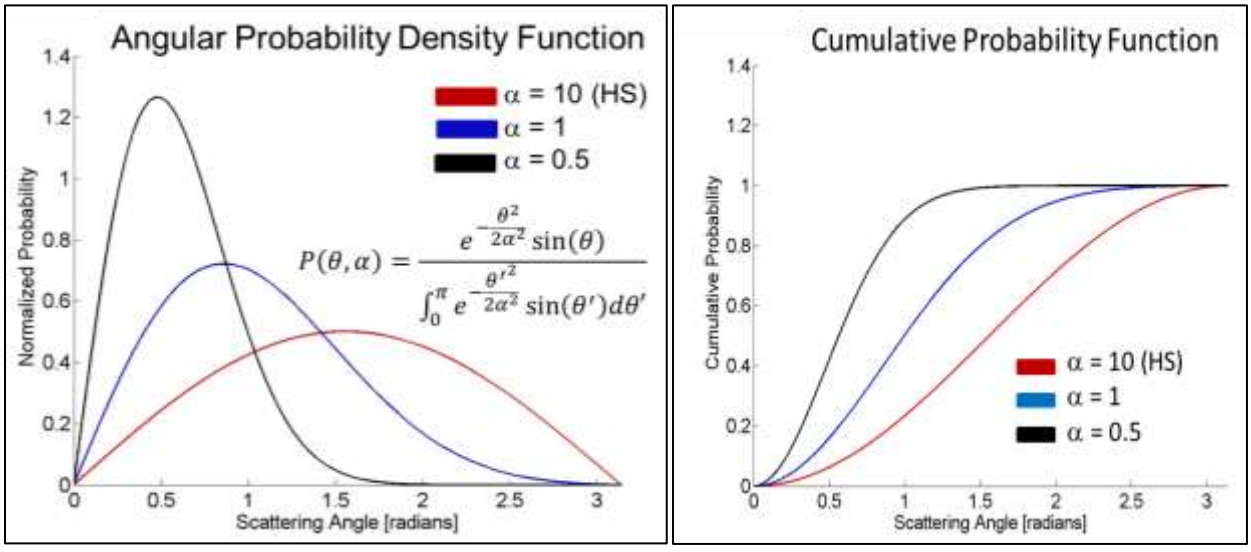

Figure 8 – Normalized PDF (right) and CPF(left) for preferential scattering utilizing a Gaussian distribution $P(\theta,\alpha)$. $\alpha = 0.5$ is very forward-peaked while $\alpha = 10$ approaches HS scattering.

3.4 Exit Criteria

As a single particle is transported, certain conditions are monitored. Once one of these conditions is met, the particle is of no further interest in the model and is discarded in favor of beginning the transportation of a new particle. This occurs until all particles in the simulation are transported. The exit criteria are based off of both the height and energy of the particle.

The first condition checked for is the height of the particle after each set transport. If the particle's height is measured to be at or below 0 km, then the particle is considered to have hit the planet's surface and transport calculations are halted. If the height of the particle is measured to be above the atmospheric escape height limit, transport of the particle was terminated. The planetary escape limit was set to be above a height where no more collisions were statistically likely of occurring (below an atmospheric density of $1x10^2$ cm^{-3}). Additionally, if the particle's energy was found to be above the escape energy, the particle was tallied as a mass loss particle. In order to determine escape energy, a planetary mass on the order of magnitude of the mass of Jupiter was used.

Additionally, the energy of the particle was checked after each collision. Every time the particle collides, it loses a percentage of its total energy. When the energy of that particle dropped below the calculated thermal energy of the planet, transportation of the particle was terminated. This indicates that the particle has collided with a significant amount of particles and has been reduced to the energy of the atmosphere around it. In other words the particle has been thermalized and is no longer distinguishable from the surrounding atmosphere. Thermalization energy was calculated using a value of planetary surface temperatures estimated from exoplanetary data (Fig.8)[6]. An approximate median value was selected of T = 1250K.

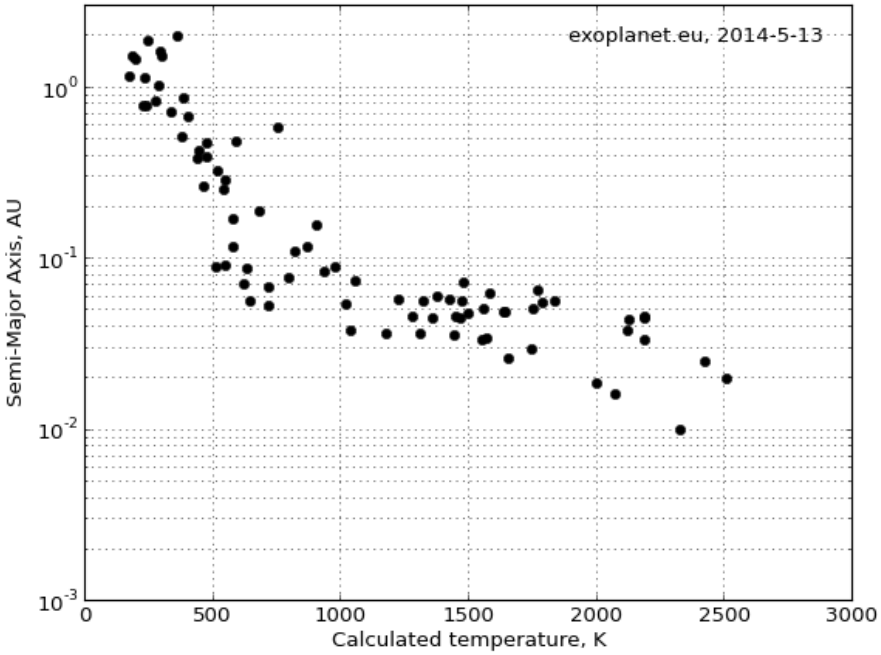

Figure 9 – Exoplanets related by semi-major axis in AU and calculated surface temperature K[6]

4 Results

4.1 ENA Energy Deposition in Atmosphere

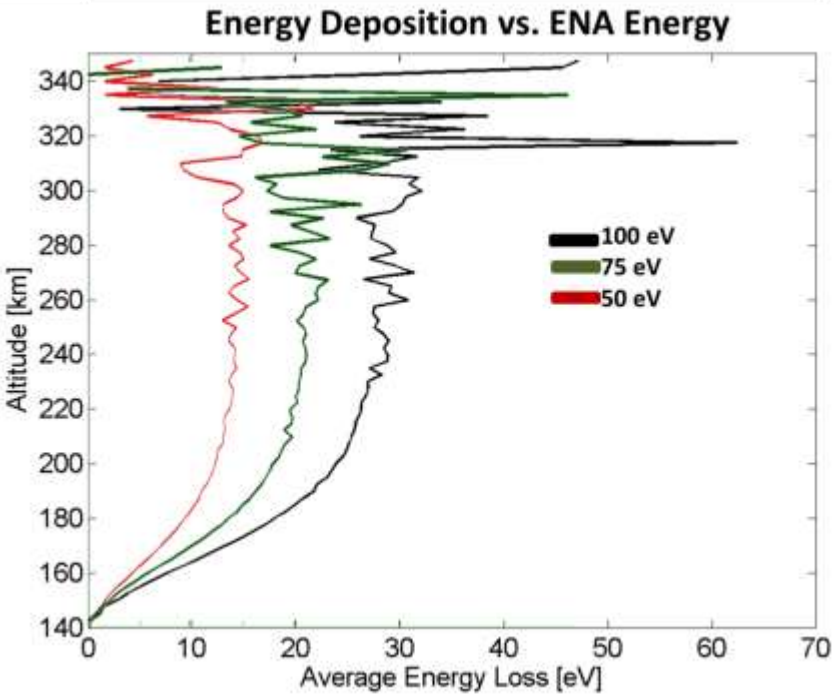

Figure 10 – Energy deposition as a function of altitude with ENAs at initial energies of 100eV (black), 75eV (green), and 50eV(red).

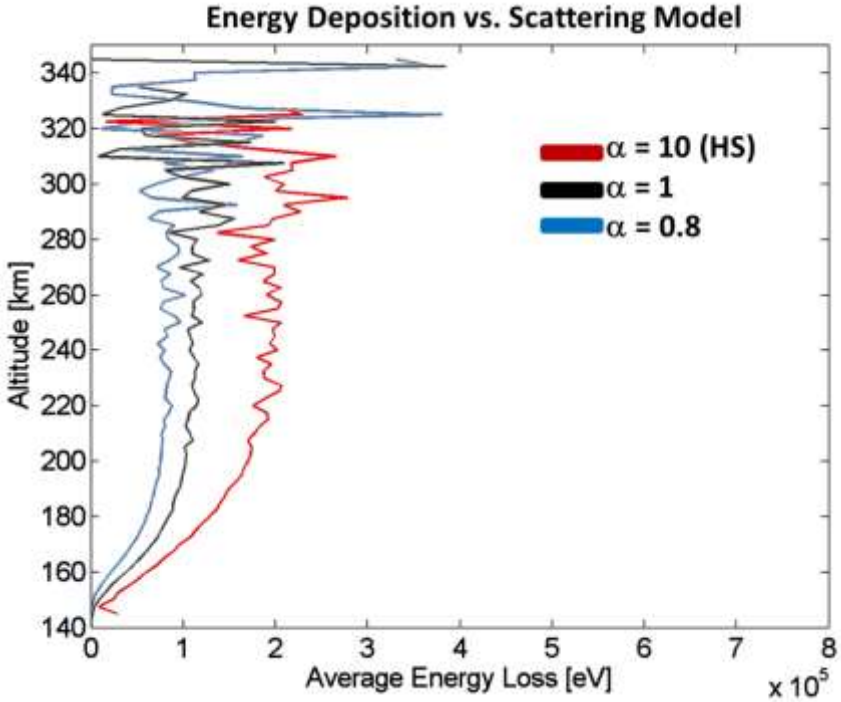

Figure 11 – Energy deposition as a function of altitude with initial ENA energy of 1 MeV in preferential scattering model. Tested α values include 10 (~HS, red), 1 (black) and 0.8 (blue).

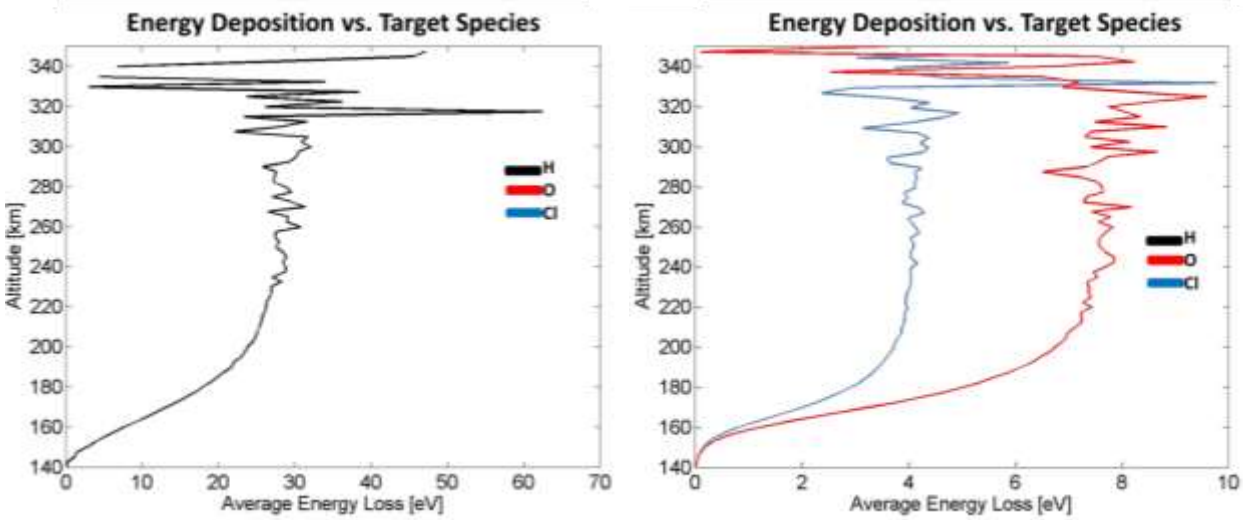

Figure 12 – Energy deposition as a function of altitude with initial ENA energy of 100 eV. Atmospheric species tested include hydrogen (black), oxygen (blue) and chlorine (red).

4.2 Reflected ENA Energy Distribution

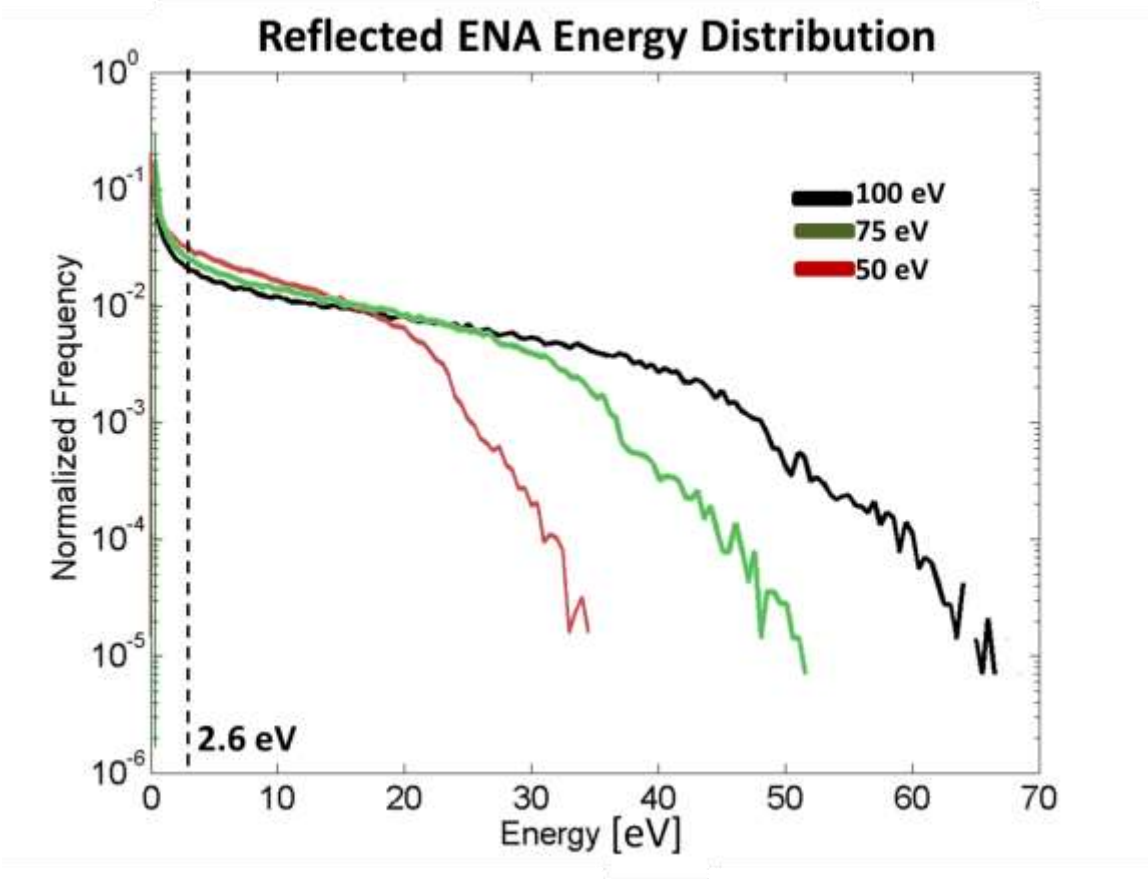

Figure 13 – Reflected ENA energy distribution with initial ENA energies of 100 eV (black), 75 eV (green) and 50 eV (red). Particles above ~2.6 eV escape.

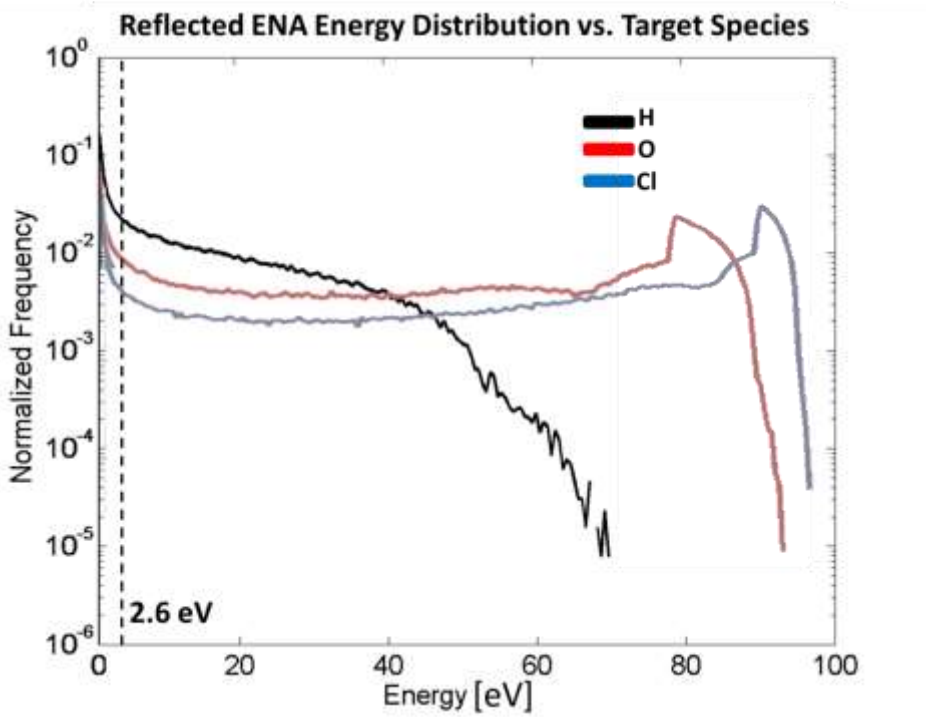

Figure 14 – Reflected ENA energy distribution with initial ENA energies of 100 eV. Atmospheric species tested include hydrogen (black), oxygen (blue) and chlorine (red). Particles above ~2.6 eV escape.

ENA Exit Criteria Distribution (Energy)

Initial Energy	Thermalized (%)	Reflected (%)	Planetary Collision (%)
100 eV	52.6	47.4	0.0
75 eV	53.4	46.6	0.0
50 eV	54.3	45.7	0.0

Table 1 – Contains ENA exit criteria data as a function of initial ENA energy at 100eV, 75eV, and 50eV. Thermalized, Reflected, and ENAs that collide with the planet surface were recorded.

ENA Exit Criteria Distribution (Target Species)

Species	Thermalized (%)	Reflected (%)	Planetary Collision (%)
Hydrogen	52.6	47.4	0.0
Oxygen	22.8	77.2	0.0
Chlorine	16.9	83.1	0.0

Table 2 – Contains ENA exit criteria data as a function of atmospheric chemical species including H, O, and Cl. Thermalized, Reflected, and ENAs that collide with the planet surface were recorded.

4.3 ENA Thermalization Height

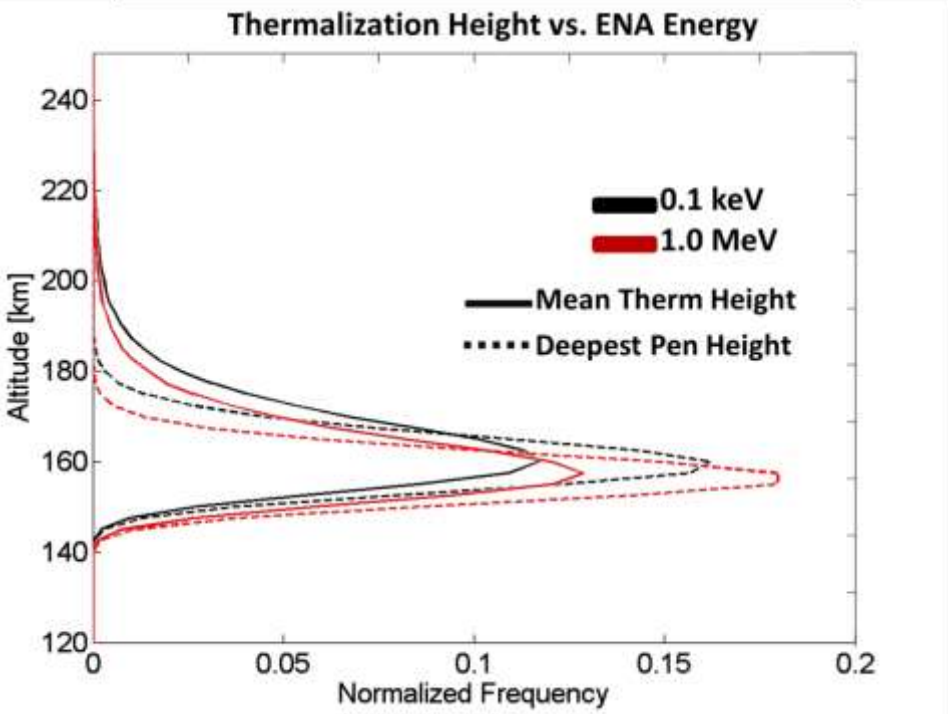

Figure 15 – ENA particle mean thermalization height and deepest mean penetration height as a function of altitude. Initial ENA energies tested include 0.1 keV (black) and 1.0 MeV (red).

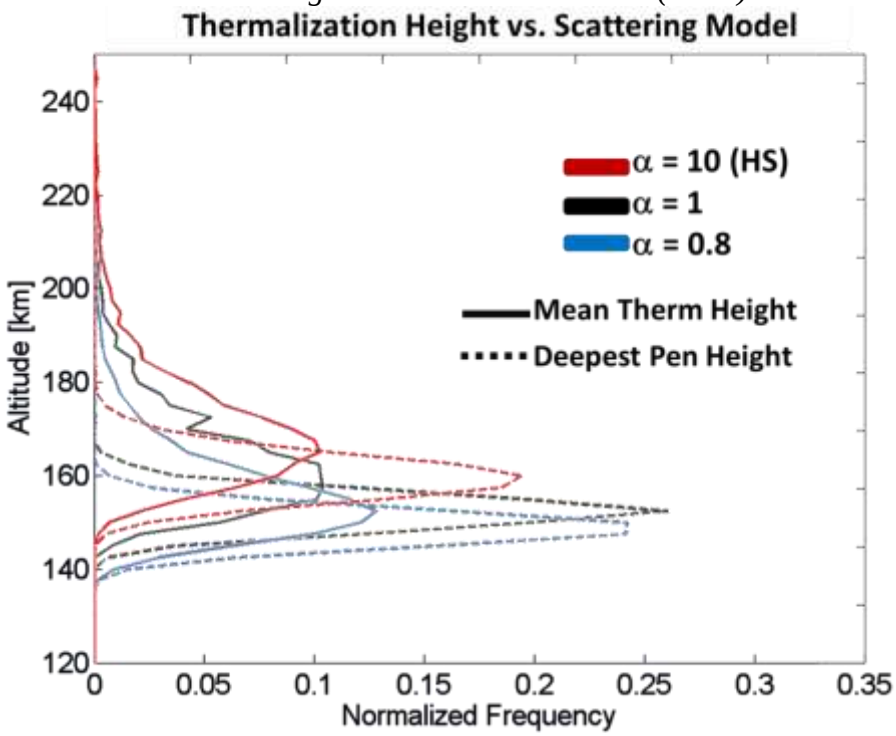

Figure 16 – ENA particle mean thermalization height and deepest mean penetration height as a function of altitude at initial ENA energy of 1 MeV in preferential scattering model. Tested α values include 10 (~HS, red), 1 (black) and 0.8 (blue).

4.4 SHP Creation Height

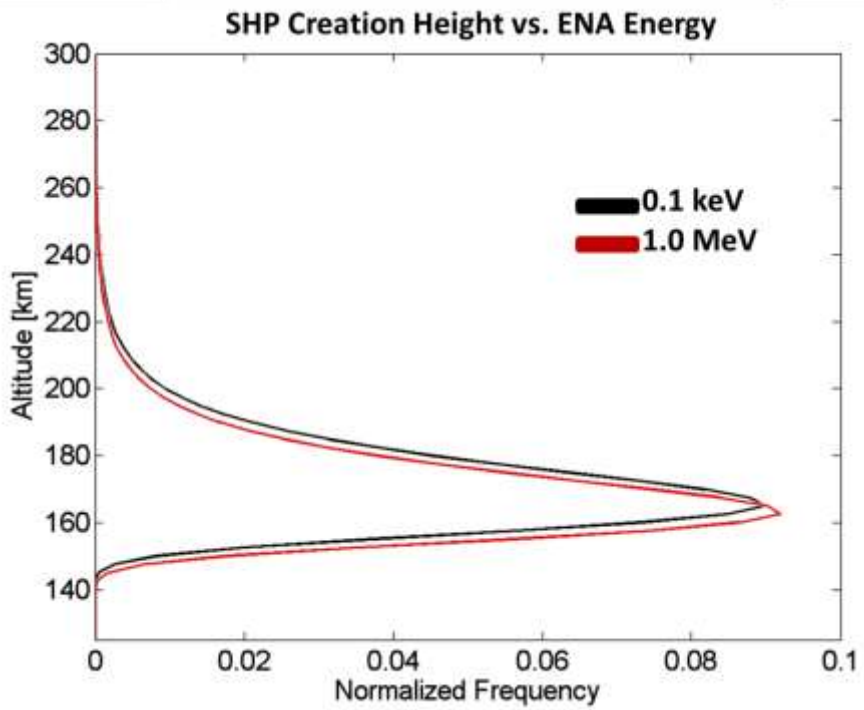

Figure 17 – SHP creation height as a function of altitude Initial ENA energies tested include 0.1 keV (black) and 1.0 MeV (red).

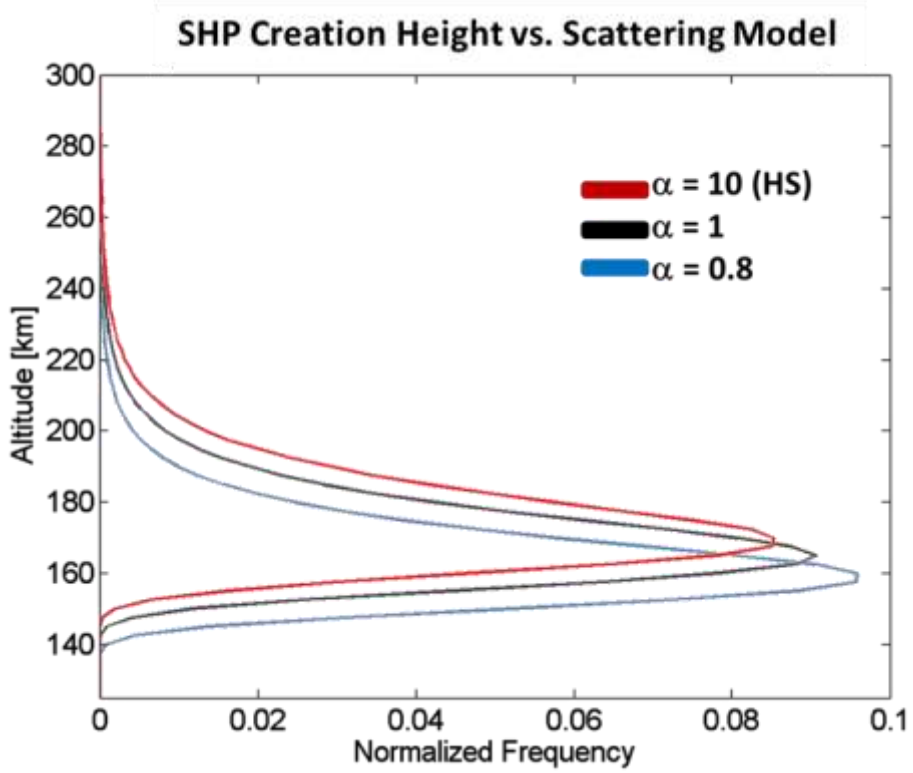

Figure 18 – SHP creation height as a function of altitude with initial ENA energy of 1 MeV in preferential scattering model. Tested α values include 10 (~HS, red), 1 (black) and 0.8 (blue).

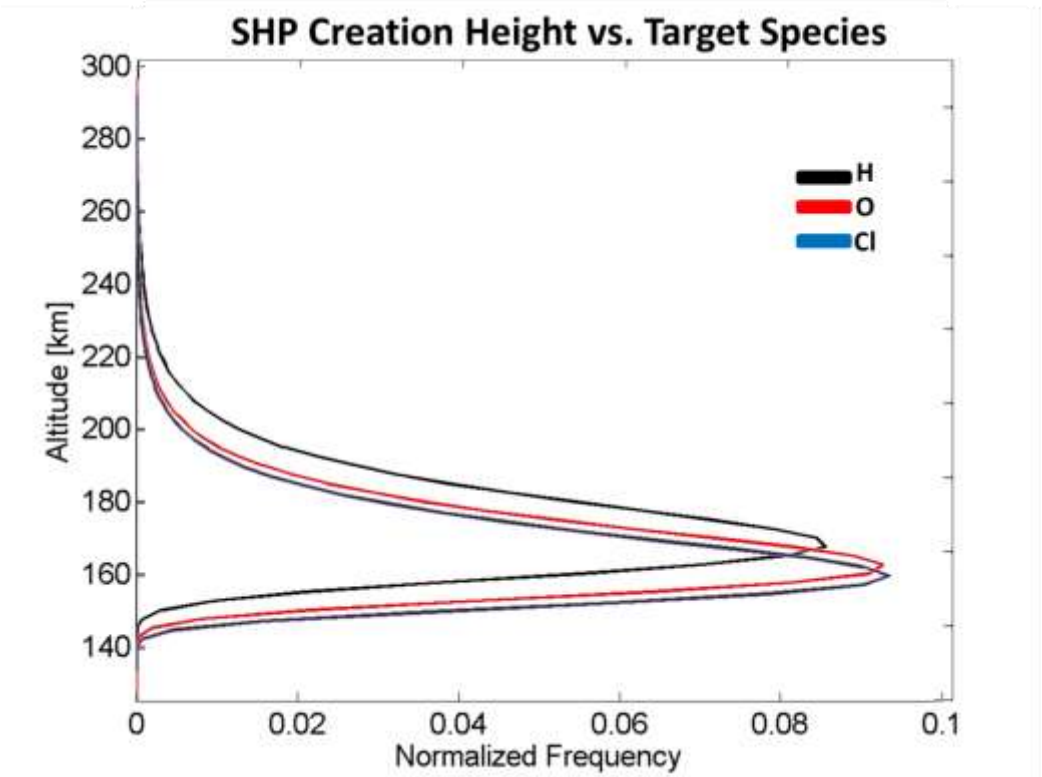

Figure 19 – SHP creation height as a function of altitude with initial ENA energy of 1 MeV. Atmospheric species tested include hydrogen (black), oxygen (blue) and chlorine (red).

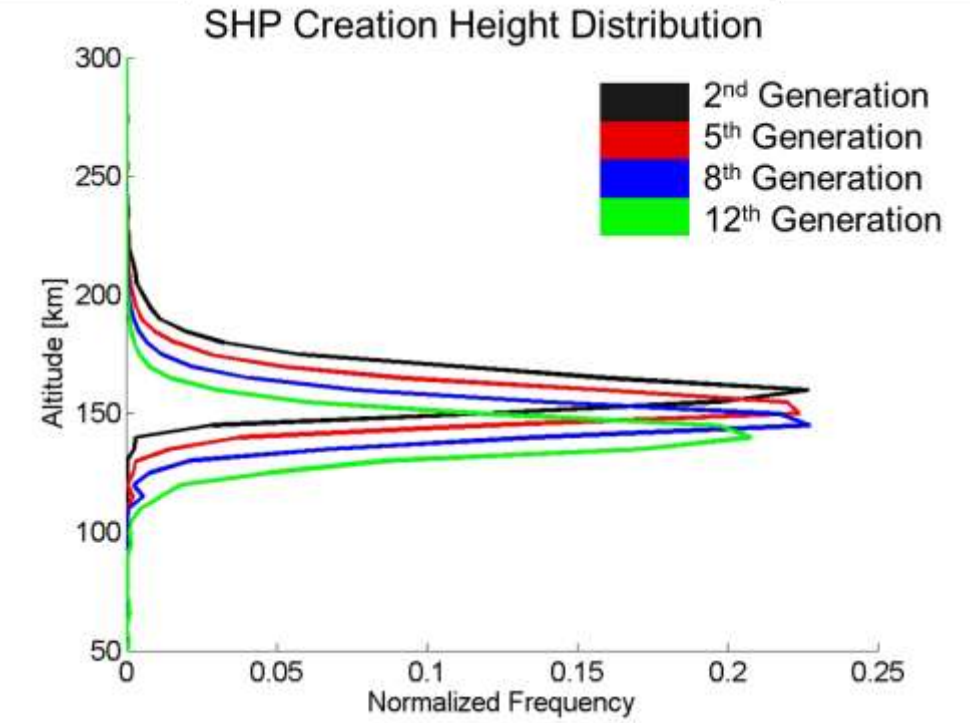

Figure 20 – SHP creation height as a function of altitude. SHP Tracking enabled, showing the 2nd (black), 5th (red), 8th(blue), and 12th (green) generations of SHP creation distributions

4.5 SHP Energy Distribution

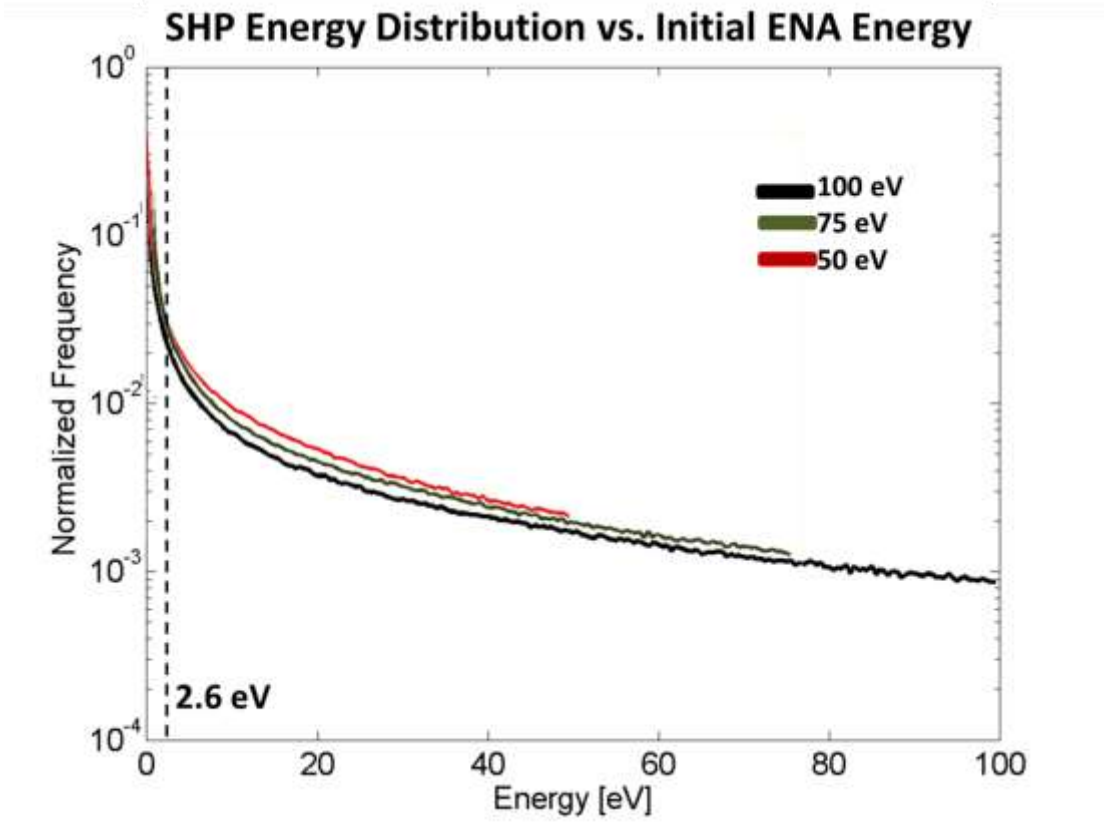

Figure 21 – Created SHP energy distribution with initial ENA energies of 100 eV (black), 75 eV (green), and 50 eV (red). Particles above ~2.6 eV have the potential to escape.

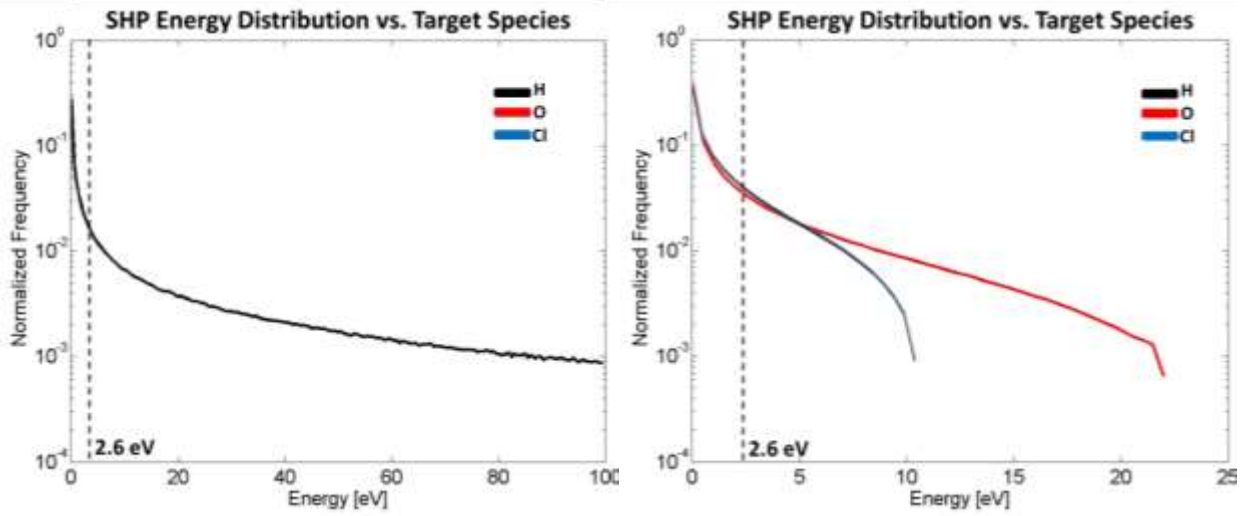

Figure 22 – Created SHP energy distribution with initial ENA energies of 100 eV. Atmospheric species tested include hydrogen (black), oxygen (blue) and chlorine (red). Particles above ~2.6 eV have the potential to escape.

Collected SHP Data (Energy)			
Initial Energy	**Collisions per ENA**	**SHP per ENA**	**SHPs Capable of Escape (%)**
100 eV	6.3	5.8	54.0
75 eV	6.2	5.6	52.0
50 eV	6.0	5.4	48.9

Table 3 – Contains SHP and Collision Data as a function of initial ENA energies of 100 eV, 75 eV, and 50eV. Collisions per ENA, SHP per ENA, and the percentage of SHPs with energies greater than the energy required for atmospheric escape were recorded.

Collected SHP Data (Target Species)			
Species	**Collisions per ENA**	**SHP per ENA**	**SHPs Capable of Escape (%)**
Hydrogen	6.3	5.8	54.0
Oxygen	24.7	19.5	35.3
Chlorine	39.8	29.0	24.5

Table 4 – Contains SHP and Collision Data as a function of atmospheric chemical species including H, O, and Cl. Collisions per ENA, SHP per ENA, and the percentage of SHPs with energies greater than the energy required for atmospheric escape were recorded.

4.6 MC Simulation

The number of Monte Carlo particles (MCPs) simulated is the largest factor for eliminating random error and signal noise within the simulation. The majority of data collected for this experiment was performed with simulations of 300,000-750,000 MCPs and normalized. The limiting factor on increasing the MCPs to improve data precision further was computing time, MCPs greater than a million taking over half a day to simulate. Additionally, certain programing alterations such as SHP tracking and preferential scattering greatly increase computing time by introducing additional particles or longer particle paths.

Noise in the data was still significant in several areas. Very few collisions occur at high altitudes due to low atmospheric density and very little energy is transferred to the atmosphere. Despite the large sample size, there is still not enough information to yield accurate statistics at very high altitudes and signal noise quickly dominates. Likewise, sources of noise due to unlikely particle energies also occur. It is unlikely that ENAs will meet escape criteria without first losing energy. Therefore, high levels of noise are present when inspecting reflected ENA energy distribution at high energy. SHPs are also unlikely to be created with energies close to that of the initial ENA energy, and noise is introduced to the SHP energy distribution at high energy.

Other sources of error arise from assumptions in the initial parameters utilized. Target and projectile radii were estimated by the Van der Waals radius. The results can also change significantly with changing effective surface temperature, exoplanetary mass, and incident ENA energy. Care was taken in order to only affect one variable at a time in order to accurately look at their effects. The escape limit was calculated utilizing an average SHP creation height of 150km and with an exoplanetary mass of the same order as Mars (639E21 kg).

5 Discussion and Implication of Results

5.1 Significance of Chosen Variables

Over the course of the project, multiple parameters were adjusted to affect change in the Monte Carlo simulation. By changing these conditions, trends in the collision model were formed and will now be discussed. The primary variables modified include incident ENA energy, the chemical composition of the atmosphere, and the scattering preference of the model. The stellar wind contains a distribution of energetic particles that can precipice ENAs with different velocities. It is important therefore, to determine how the initial velocity of these precipitated ENAs impact the model. This is done by testing initial ENA energies in a broad range from 50 eV to 1MeV.

The chemical composition of the atmospheric model is also modified. Planetary and exoplanetary atmospheres contain many species of gases. Larger, heavier molecules will interact with the ENAs differently than lighter atmospheric particles, so different chemical species were substituted into the model to determine differences in the simulation's output. Lastly, the model itself was altered slightly to allow for forward scattering to be preferentially favored. Realistically, the ENA-atmosphere interactions are quantum in nature and should utilize quantum cross-sections. However, the implementation of such interactions can be difficult. By introducing preferential scattering, some aspects of quantum mechanical scattering can still be explored.

5.2 Impact of Initial ENA Energy

By changing the initial energy of incident ENAs, several changes occur within the simulation. As energy increases, energy deposition increases at higher altitudes (Fig. 9). All elastic collisions in the model transfer a portion of the total energy of the projectile ENA. Therefore, the model correctly demonstrates that higher initial energies leads to greater amounts of energy introduced into the system. In the reported results at altitudes lower than 200 km the energy deposited in the system begins to converge independently from the initial ENA energy.

Increasing initial ENA energy also changes the energy distributions of reflected ENA particles and created SHP (Fig. 12 and Fig. 20). Both the reflected ENA and created SHP figures indicate that higher initial energies yield a greater range of potential energies within the distribution. However, a more important result is that by increasing initial ENA energy the number of reflected ENA particles increases while the percentage of SHPs capable of atmospheric escape also expands (Table 1 and Table 3). By increasing initial ENA energy, the percentage of reflected ENAs was increased by 1.7% while the number of SHPs with energies great enough to escape increased by 5.1%. ENA energy has a much smaller effect on SHP creation height and ENA thermalization height (Fig.14 and Fig 16). Even by introducing ENAs with energies four orders of magnitude greater, only small changes in SHP creation and thermalization heights can be seen, slightly pushing the centers of these distributions lower in the atmosphere. By comparison, by tracking SHPs through a process similar to the one used to tracking ENAs it becomes apparent that each progressive production generation of SHPs are created deeper within the atmosphere (Fig. 19).These results confirm the generally accepted idea that higher-energy particles are more capable of inducing the non-thermal mass loss in an atmosphere than slower, less energetic particles.

5.3 Impact of Atmospheric Chemical Composition

Next, several different gases were used to determine how changes in atmospheric composition affect atmospheric mass loss. Hydrogen, oxygen, and chlorine gases were used, with hydrogen being the lightest and the smallest and chlorine the heaviest and largest. These particles were represented in the model by altering the atmospheric target particle masses and Van der Waals radii. Changes in the model were significant, with oxygen and chlorine both dramatically decreasing the amount of energy the model deposits in the atmosphere (Fig. 11). This change arises from a dramatic shift in the $\rho = \frac{m_p}{m_t}$ ratio utilized to calculate the energy transferred to atmospheric particles. Due to conservation of momentum vectors, when a light particle collides with a heavier stationary particle the velocity of the heavier particle is reduced by the same factor that the mass of the heavier particle is increased by. Overall, the energy transferred will be decreased by the same factor.

This changes the model in several ways. By changing the atmospheric gas from hydrogen to chlorine, the number of total collisions the ENAs experience increased from 6.3 to 39.8 per MCP (Table 4). As a result, the number of SHPs produced increased dramatically. However, the maximum SHP energy was decreased by a factor of ten, (Fig. 21), reducing the fraction of SHPs capable of escape from 54% with a hydrogen atmosphere to 24.5%. The number of ENAs reflected also dramatically climbs by 35.7%, (with an equal reduction in thermalized ENAs) most likely as a result of the larger cross sections increasing the likelihood for scattering at higher altitudes (Table 2). The energy distribution of the escaping ENAs is also heavily altered. Both the oxygen and chlorine atmospheres experienced peaks in energy distribution at energies close to 80% or 90% of initial ENA energy (Fig. 13). Finally, the SHP creation height distribution shifts to lower altitudes when more massive atmospheric gases are present, further reducing the SHP escape probability Fig. 18).

5.4 Impact of Preferentially Scattering Model

Finally, a preferentially forward scattering model was designed in order to create a model that more closely simulates quantum cross sections. The distribution function used was designed with a variable α in order alter the model from the HS approximation (α = 10) to increasingly forward scattering particles. After the new model was implemented, several changes became immediately noticeable. As α decreases and scattering becomes less isotropic, the energy deposition at high altitudes to ENA-atmosphere interactions also decreases (Fig. 10). Additionally, mean thermalization height, deepest penetration height, and SHP creation height, all shift to lower altitudes (Fig, 15 and Fig. 17). These changes can be explained by the mechanisms responsible for hard-sphere energy transfer. The θ dependence of the energy transfer (equation 18 of section 2.5) effectively minimizes the possible transfer energy when forward scattering is highly preferential. Physically, what this means is that since the scattering angle remains small, the ENA ballistic path isn't greatly affected by the collision leading one to consider the case of an indirect or glancing collision where not much energy is imparted to the atmospheric particles. As a result, ENAs were more likely to penetrate deeper into the atmosphere before thermalizing due to a downwardly-favorable initial orientation and due to the fact that the collisional transfer energy is greatly reduced.

5.5 Application of Results to Exoplanetary Hot Jupiters.

The results of this study can be applied directly to the study of Hot Jupiter exoplanets and can be used to hypothesize potential atmospheric conditions. Due to Hot Jupiters' proximity to their parent stars, they survive under extreme conditions with high surface temperature and high fluxes of solar winds, potentially leading to rapid atmospheric evolution. Higher ENA fluxes and energies indicate rapid energy deposition in the atmosphere, along with higher fluxes of escaping SHPs due to greater escape potential. Additionally, the ENAs will collide with more particles before thermalization and will therefore produce more SHPs.

Due to their high surface temperatures, it will not be uncommon for Hot Jupiters to possess few low-mass volatiles. This means that many exoplanetary ENA interactions that occur will happen with heavier gases such as Fe, FeO, Mg, Na, O, O_2, SiO, SiO_2, H_2S, and CO_2[28,29]. If the trends identified in our model continue to hold true, than it is anticipated that these heavier elements will reflect a large number of ENAs, increasing the atmospheric opacity due to low energy transfer and high cross-sectional areas.

Finally, the forward scattering model can be utilized instead of more complex quantum mechanical collision models that often require the development and implementation of a different cross-section for each different type of target-projectile collision.

6 Conclusion

This study has analyzed the effects of several variables and conditions impacting atmospheric mass loss rates due to ENA production and atmospheric injection including initial ENA energy, atmospheric chemical species, and preferential scattering orientations. Key changes in the Monte Carlo model were observed in relation to the tested variables. Alterations in the ENA reflection coefficient were observed, which increased with decreasing initial ENA energy and increasing atmospheric chemical species atomic number. SHP creation and ENA thermalization occurred at relatively similar atmospheric depths and were shifted more deeply into the atmosphere by increasing initial ENA energy, increasing the radius and mass of the atmospheric gas, and by introducing a forward scattering model. Finally, energy deposition rate was heavily affected by all three variables with the greatest energy deposition appearing in the models with high initial ENA energy, isotropic hard sphere scattering, with a hydrogen atmosphere.

Future work on this model should be directed to implementing alternative atmospheric density distribution and quantum collision cross sections in order to improve the variety of data provided and the usefulness of the model with the goal of improving the understanding of mass loss rates due to ENA reflection and SHP escape.

The further development and exploration of atmospheric Monte Carlo mass loss models will play a significant role in our understanding of exoplanetary and planetary atmospheric formation, evolution, and destruction. Due to technological limitations and great distances, atmospheric modeling is one of the strongest modern tools in order to determine the properties of such distant objects.

References

[1] Gossin P. (2002). *Literature and Science: Antiquity*. Encyclopedia of Literature and Science (pp. 235-237). Westport: Greenwood.

[2] Aquilecchia G. (2013). *Giordano Bruno*. Encyclopedia Britannica (Online). Chicago: Encyclopedia Britannica.

[3] Mayor M, Queloz D. (1995). *A Jupiter-mass Companion to a Solar-type Star*. Nature, 378: 355-359.

[4] Seager S, Deming D. (2010). *Exoplanet Atmospheres*. Annu. Rev. Astron. Astrophys, 48: 631-72.

[5] Gray D. (1997). *Absence of a Planetary Signature in the Spectra of the Star 51 Pegasi.* Nature, 385: 795-796.

[6] Irap I, Chauvin C, Mancini M, Sidaner P. (2014). *The Extrasolar Planets Encyclopedia*. Jean Schneider Observatoire de Paris. <http://exoplanet.eu/>.

[7] Cassan A, Kubas D, Beaulieu M, et al. (2012). *One or More Bound Planets per Milky Way Star from Microlensing Observations.* Nature, 481: 167-169.

[8] Struve O. (1952). *Proposal for a Project of High-Precision Stellar Radial Velocity Work.* The Observatory. 72: 199-200.

[9] Seager S, Sasselov D. (2000). *Theoretical Transmission Spectra During Extrasolar Giant Planet Transits*. The Astrophysical Journal, 537: 916-921.

[10] Charbonneau D, Brown T, Latham D, Mayor M. (2002). *Detection of Planetary Transits Across a Sun-like Star.* The Astrophysical Journal, 529: L45.

[11] Charbonneau D, Brown T, Noyes R, Gilliland R. (2002). *Detection of an Extrasolar Planet Atmosphere*. The Astrophysical Journal, 568: 377-384.

[12] Salby, M. (1996). *Composition and Structure, Thermodynamics of Gases.* Fundamentals of Atmospheric Physics (pp. 3-77). New York: Academic Press.

[13] Zendejas J, Segura A, Raga A.C. (2010). *Atmospheric Mass Loss by Stellar Wind from Planets Around Main Sequence M Stars*. Icarus, 210: 539-544.

[14] Lammer H, Lichtenegger H, Kolb C, Bauer S.J. (2003). *Loss of Water from Mars: Implications for the Oxidation of the Soil*. Icarus, 165: 9-25.

[15] Kallio S, Lushmann J.G. (1997). *Charge Exchange Near Mars: The Solar Wind absorption and Energetic Neutral Atom Production*. Journal of Geophysical Research, 102: 183-197.

[16] Lewkow N, Kharchenko V. *Database for Imaging Transport with Energetic Neutral Atoms (ENAs)*. Conducted lecture.

[17] Gu P.C., Lin D, Bodenheimer P. (2003). *The Effect of Tidal Inflation Instability on the Mass and Dynamical Evolution of Extrasolar Planets with Ultrashort Periods.* The Astrophysical Journal, 588: 509-534.

[18] Lecavelier des Etangs A, Vidal-Madjar A, McConnell J.C., Hebrard G. (2004) *Atmospheric Escape from Hot Jupiters*. A&A. 418: L1-L4.

[19] Lecavelier des Etangs A, Bourrier V, Wheatley P, Dupuy H, Sing D.K. (2012). *Temporal Variations in the Evaporating Atmosphere of the Exoplanet HD 189733b*. A&A, 543: L4.

[20] Kittel C, Kroemer H. (1980). *Thermal Physics, Second Edition*. New York: W.H. Freeman and Company.

[21] Taylor J. (2005). *Classical Mechanics.* New York: University Science Books.

[22] Griffiths, D. (2005). *Introduction to Quantum Mechanics, Second Edition.* New Jersey: Pearson Prentice Hall.

[23] Landau L.D., Lifshitz E.M. (1976). *Course of Theoretical Physics Volume 1: Mechanics, Third Edition.* Burlington: Elsevier Butterworth-Heinemann Ltd.

[24] Dunn W, Shultis J.K. (2011). *Exploring Monte Carlo Methods*. Burlington: Elsevier Butterworth-Heinmann Ltd.

[25] Krasnopolsky, V. (2002). *Mars' Upper Atmosphere and Ionosphere at Low, Medium, and High Solar Activities: Implications for Evolution of Water.* Journal of Geophysical Research, 107: E12.

[26] Fox J. (2009). *Morphology of the Dayside Ionosphere of Mars: Implications for Ion Outflows.* Journal of Geophysical Resarch, 114: E12.

[27] Feldman U, Schuhle U, Widing K.G., Laming J.M. (1998). *Composition Above the Solar Equator and the North Pole as Determined from Spectra Acquired by the SUMER Instrument on SOHO*. The Astrophysical Journal, 505:999-1006.

[28] Miguel Y, Kaltenegger L, Fegley B, Schaefer L. (2011). *Compositions of Hot Super-Earth Atmospheres: exploring Kepler Candidates*. The Astrophysical Journal, 742: L19.

[29] Fortney J.J, Shabram M, Showman A.P., Lian Y, Freedman R.S., Marley M.S., Lewis N.K. *Transmission Spectra of Three-Dimensional Hot Jupiter Model Atmospheres*. ApJ.

Appendix

Computational model coded in MATLAB attached to the following pages for the Classical, Forward Scattering, and SHA Tracking models developed.